The Measurement Capabilities of Wide-Swath Ocean Altimeters

Ernesto Rodriguez and Brian D. Pollard
Jet Propulsion Laboratory
California Institute of Technology
Pasadena, CA 91109

Introduction

The High-resolution Ocean Topography Science Working Group (HOTSWG) meeting held in Washington D.C. in April of 2001 examined the capabilities of various instruments for meeting future science needs for high resolution ocean topography.

Among the instruments considered was the Wide-Swath Ocean Altimeter (WSOA), an interferometric radar capable of providing ocean topography over 200 km swaths. The design presented during the April '01 HOTSWG meeting was a design which had been proposed by JPL for inclusion as a demonstration mission together with the proposed Jason-2 mission. Due to limitations in the Jason bus, the instrument shown did not represent the ultimate potential of the technique for future missions, such as the NPOESS platform. In addition, it was repeatedly stated during the meeting that, even for a demonstration mission, it would be highly desirable if the random height errors could be reduced.

In this chapter, we review the WSOA system concept and capabilities, and address the concerns of the HOTSWG. In addition to issues identified by the HOTSWG, E. Walsh (private communication) has brought up a concern which he thinks limits the accuracy of any off-nadir height measurement instrument. Since the answer to his concern highlights the difference between the WSOA and more conventional altimeters, we think it is useful to present the resolution to the HOTSWG.

This chapter is divided as follows:

- **Overview of the WSOA Instrument:** In this section, we review the WSOA system concept, its predicted perfomance integrated with the Jason-2 altimeter.
- **Design Improvements to the Jason-2 WSOA Demonstration Mission:** After the April '01 meeting we reexamined the WSOA design and found improvements in the processing techniques and the mode of operation which can be accommodated with the Jason-2 bus. These improvements help to significantly reduce the random measurement noise.
- **Potential Design Changes for Future Missions:** This section addresses design changes which could be made with the current technology, but require the use of a different platform to fly the WSOA instrument. In this section, we show that, with currently available radar and interferometric mast technology, and with a platform capable of handling the products and moments of inertia of the WSOA instrument, single pass height performance accuracy comparable to nadir altimeters can be achieved over the entire swath. The performance improves even further if it is taken into account that the WSOA will revisit most points on the surface at least twice within a 10 day cycle.
- **Is Off-nadir Altimetry Inherently Limited?** This section addresses concerns raised by E. Walsh, and shows that the WSOA concept is qualitatively and quantitatively different from traditional altimetry.

The WSOA Measurement Concept

In order to map ocean mesoscale phenomena adequately, it is necessary to be able to resolve phenomena which are on the order of the Rossby radius of deformation (a conservative value would be on

the order of 30km) and have a typical lifetime on the order of a month. It is not possible to reconcile both of these requirements with a single nadir looking altimeter: the TOPEX altimeter has a repeat cycle of 10 days, but an equatorial separation of 300 km. Given a sufficient number of satellites, it is possible to meet these requirements, but at the cost of coordinating and launching multiple platforms, as well as cross-calibrating different systematic errors due to orbit and instrument biases.

The Wide Swath Ocean Altimeter (WSOA) concept is an attempt to meet the requirements using a single platform. The WSOA consists of a suite of instruments: a conventional nadir altimeter (Ku and C-band nadir altimeters, 3-frequency radiometer, and GPS receiver) supplemented by a Ku-band radar interferometer [Rodriguez and Martin, 1992] [Rodriguez et al., 2001]. Figure 1 shows a diagram of the integrated instrument. The nadir altimeter is used for high precision basin scale measurements, for the estimation of ionospheric and tropospheric delays, and for the calibration of the interferometer.

The radar interferometer illuminates 100 km swaths on either side of the nadir track using right and left-looking beams. The intrinsic cross-track resolution varies from approximately 670 m in the near range to about 100 m in the far range. The along-track resolution is given by the azimuth beamwidth, and is approximately 13.5 km. In order to have spatially uniform resolution cells, and to reduce random measurement error, the final measurements are averaged to 15 km resolution cells.

The 200 km swath enables the WSOA to achieve near global coverage with a single instrument. Figure 2 shows a comparison of the coverage obtained by two TOPEX-like altimeters, separated at the equator by 150 km, and the coverage obtained by a single WSOA. The height field shown is from the Los Alamos National Laboratory 0.1 degree eddy-resolving circulation model. The WSOA results shown are the products of a measurement simulator which includes random and systematic measurement errors.

Another advantage of the 200 km swath is that, in contrast with a nadir looking altimeter, a typical point on the ocean surface will be imaged at least twice within a 10-day repeat period, and often more frequently. Figure 3 shows the number of times the North Atlantic is imaged by the instrument. The multiple looks at the same point can be used to improve temporal sampling, but, perhaps more importantly, to reduce random measurement errors by averaging, optimal interpolation, or assimilation. Typically, one observes that the effective random measurement error is reduced by a factor of $1/\sqrt{2}$, or better.

The high accuracy requirements for ocean topography measurements implies that the measurement error budget must be thoroughly understood. The errors for interferometric measurements and for the WSOA in particular are described in detail in [Rodriguez and Martin, 1992] [Rodriguez et al., 2001], so we limit ourselves here to a brief statement of results. The WSOA errors can be derived into three components: random errors, media errors, and platform roll errors. The random error contribution depends on the system signal to noise ratio (SNR), on the length of the interferometric baseline, and on the processing used. At the HOTSWG meeting, we presented the random height error coresponding to an implementation of WSOA designed to fit on the Jason platform constraints, which limit the baseline length to 6.4 m. The predicted performance is shown in the second column of Table 1a. We have subsequently refined our operational mode and processing algorithms, so that the single pass random height accuracy has improved significantly. These results are presented in the next section. During the HOTSWG meeting we also showed that, after mosaicking the data over one cycle, and applying the cross-over calibration described below, the mosaicked data root mean squared error dropped to 3.2 cm. Since the mosaicking algorithm is linear, we expect that the performance using the improved WSOA described in section 3, will improve linearly with the improved random noise performance. This remark applies as well to the estimation of geostrophic velocity.

The WSOA interferometer does not directly measure tropospheric, ionospheric, and EM bias corrections, but uses the corrections from the nadir altimeter. Spatial variability of the ionosphere, troposphere, wave and wind fields over the scales of the swath will induce residual height errors. To

quantify these residual errors, we use the TOPEX along-track measurements of these quantities to estimate spatial variability of the corrections. Since these errors have a latitudinal dependence, we subdivide the data into 10 degree latitude bands. The result for the total (tropospheric, ionospheric, and EM bias) error for the global average, and the worst and best latitude bands is presented in Figure 4.

Finally, the lack of knowledge in the spacecraft roll angle induces height errors. In order to remove these errors, we have deviced a calibration scheme which uses ascending and descending WSOA data at cross-over regions to estimate and remove the roll errors (see Figure 5). In order to validate the accuracy of the calibration technique, we have performed a simulation using one year of LANL circulation model data and a set of spacecraft roll characteristics for the Jason platform provided to us by CNES/Alcatel. An example of the resulting corrected height fields is shown in Figure 2b. As mentioned above, the total height root mean squared error, including random and roll errors, is 3.2 cm.

One of the principal advantages of the WSOA measurements is that one can obtain the two-dimensional sea surface, rather than just the traditional along-track profiles measured by nadir altimeters. The availability of a two-dimensional height field allows the calculation of surface topography derivatives in the zonal and meridional directions. This means that it is possible to estimate the full **vector** geostrophic velocity everywhere WSOA measurements are available, rather than the single component of the velocity measured by a nadir altimeter. Figure 6a shows an example for the magnitude of the two-dimensional geostrophic velocity for the topography presented in Figure 2b. The results of the LANL based simultaion show that the root mean squared error for the U and V components of the geostrophic velocity for the mosaicked data is 4.7 cm/s and 5.9 cm/s, respectively. One can then use the time series of vector velocities to obtain estimates for the Reynolds stresses sampled at high resolution (Figure 6c). Similarly, the Laplacian of the height field can be used to estimate the geostrophic relative vorticity (Figure 6b). The accuracy for these derived fields has been obtained using simple mosaicking, which is a simplistic model for the optimal estrimation for these quantities. The estimation accuracies using more sophisticated techniques is currently under investigation.

Design Improvements to the Jason-2 WSOA Demonstration Mission

The measured interferometric phase is noisy because the two interferometric channels are not perfectly correlated. In the design presented at the April '01 HOTSWG, the following were the sources of signal decorrelation:

- Thermal noise.
- Geometric decorrelation: this is due to the fact that at boresight, the surface will speckle slightly differently for each receiver channel.
- Angular decorrelation: this is due to the fact that iso-phase lines are not aligned with iso-range lines.
- Misregistration: for the simple design, the returns were not completely aligned on the ground away from the center of the swath.

As an example of the relative contribution of each source of decorrelation, Figure 7 shows the different contributions for the design presented at the April '01 HOTSWG meeting.

After some thought, we have realized that, for a minor computational penalty on the on-board processor, it is possible to eliminate two of the sources of decorrelation: the geometric and misregistration correlations.

In addition to improving phase noise, it is possible to reduce height noise by making the measured interferometric phase difference more sensitive to height variations. This can be accomplished by extending the interferometric baseline. However, it can also be accomplished by transmitting from both interferometric antennas, as described below.

The following subsections describe how these sources of error can be incorporated into the WSOA design, the penalties incurred in doing so, and the gains in performance.

Improving Channel Co-Registration

Due to the fact that the two interferometric receivers are separated by the interferometric baseline, signals from the same point on the ground will arrive at different times at the receivers. It is possible to add a single delay between the channels so that the signals are corregistered for a given incidence angle. However, residual misregistration will still occur away from the selected direction.

In order to perform channel registration, conventional synthetic aperture radars (SAR) use an interpolation algorithm using a finite interpolation kernel. However, in order to preserve phase accuracy, the kernel length is not small, and the procedure is computationally expensive.

The WSOA is a real aperture radar, and we show in Appendix A that in this case the interpolation of the two channels can be performed add a small computational cost using the chirp-z or chirp scaling algorithm [Rabiner, et al., 1969] [Raney, et al., 1994] . In contrast to conventional SAR's, the co-registration during range compression does not disturb subsequent synthetic aperture image formation.

As shown in Appendix A, the computational cost of using chirp-scaling for co-registration is small and can be easily incorporated into the current WSOA design.

The Wavenumber Shift for WSOA

The source of geometric decorrelation is the fact that the interferometric phase is not constant for all the scatterers within a given resolution cell. This variation in the interferometric phase causes the total interferometric contribution from that cell to add slightly incoherently, thus reducing the signal correlation.

Gatelli et al. [1994] had an insight: suppose that one were dealing with monochromatic signals, and chose the wavelengths of the two channels to be such that the projected wavevectors on the ground are identical for both channels. In this case, the interferometric phase would be constant for all scatterers in the resolution cell, and the returns would add coherently.

When dealing with a finite bandwidth signal, things are a bit more complicated, but Gatelli et al. [1994] provide a solution: take the signal from both channels and shift the spectra in such a way that the appropriate wavelengths are multiplied together so that the phase variation over the resolution cell is canceled. This spectral shift means that noise is now brought into the processing bandwidth. In order to remove this additional noise, Gatelli et al. propose to use a low-pass filter so that only the parts of the spectra which overlap contribute to the interferometric return. The penalty for this low-pass filter is a loss in resolution, but this loss is usually small and acceptable.

The wave-number shift proposed by Gatelli et al. [1994] applies to SAR's, where the angular variation of the resolution cell in the azimuth direction is very small, so that iso-range and iso-phase lines can be consireded to be aligned. However, this situation no longer applies for the WSOA: since it is a real aperture system, significant deviations can occur between these two sets of lines. Viewed in another way, this is equivalent to saying in the monochromatic case that two wavelengths can be found to cancel the interferometric phase for one given azimuth direction, but not for all.

In Appendix B, we show the effects of implementing the wave-number shift for WSOA: the geometric correlation term can be made to disappear, but the angular correlation term remains. Nevertheless, the performance gains are still significant enough to warrant the inclusion of this algorithm in the WSOA on-board operation.

The operations involved in implementing the wave-number shift consist of shifting the spectrum of the two signals after range compression by multiplying both with a phase ramp in time, followed by FIR filtering of the signals. The spectral shift can be combined with the last step of the chirp-scaling algorithm, which also involves multiplying each signal sample with a complex number, so that no computational penalty is involved. There is a computational penalty involved in FIR filtering the signals, but for small filter kernels, as will be the case for WSOA, the number of computations is small compared to performing the range compression.

A study of the modifications required show that the on-board processor already prototyped for WSOA is capable of accommodating both chirp scaling and the wavenumber shift.

Ping-Pong Interferometric Operation for WSOA

If one transmit out of one antenna and receives in both, the interferometric phase difference will be given by

$$\Phi = 2kr_1 - k(r_1 + r_2) = k(r_1 + r_2) \approx kB\sin\theta$$

However, if it were possible to transmit and receive out of one antenna, followed by transmitting and receiving out of the other one (which is called ping-pong mode in conventional interferometry), the interferometric phase would be

$$\Phi = 2kr_1 - 2kr_2 \approx 2kB\sin\theta$$

i.e. operating in ping-pong mode results in obtaining an effective baseline which is twice as long as the physical baseline.

All things remaining the same, one could think of implementing ping-pong mode by alternating the antenna used for transmit with every pulse. However, this simple approach will not work: it is well known that for distributed scatterers, such as the ocean surface, pulses which are separated by more than one-half an antenna length are not correlated. Therefore, in order to implement ping-pong mode one must transmit bursts of pairs of pulses, with the pulse separation being such that the two pulses are correlated and fit in the same return window.

In order to do this and retain constant average power, the pulse length of the two pulses must be halved, leading to a decrease in the signal-to-noise ratio (SNR). However, it can be shown that the height noise is proportional to the square root of the SNR, while the proportional to the inverse baseline length so that roughly a factor of $\sqrt{2}$ performance gain can be achieved.

An additional concern when using close pulse pairs for ping-pong mode is that the range ambiguities will increase, degrading performance. Similarly, one must be careful to chose the pulse repetition frequency and the pulse spacing so that both returns fit with the return window without interference, and there is no interference with the nadir altimeter.

A detailed calculation shows that for the proposed WSOA system, a pulse spacing can be found such that the range ambiguities from the second pulse does not significantly increase the range ambiguity level: in practice, the range ambiguity is always dominated by the 0th, opposite side ambiguity. Further reduction of ambiguity contamination can be achieved by using opposite direction chirps for each pulse. Similarly, a PRF can be found such that ping-pong operation can occur simultaneously with the nadir altimeter.

The real cost of using ping-pong mode is the increased load on the on-board processor. One can show that a pulse length can be used such that half the range samples are required for the compression of each channel. However, using ping-pong mode introduces an additional calibration error on the transmit channel which canceled out in "standard" operation. This additional transmit phase imbalance can be calibrated using the null-baseline interferogram, but at the cost of roughly doubling the required number of range compressions. This will increase the processor power requirements, but we estimate that this mode could be demonstrated in the Jason-2 mission as an experimental mode.

Performance Improvements

We have taken into account the changes proposed above and calculated the expected performance for instantaneous mapping for an interferometric baseline of 6.4 m, assuming a single-transmit chirp length of 90 μsec, and a ping-pong chirp length of 45 μsec. The ocean σ_0 was assumed to be in the 95% percentile (only 5% darker ocean conditions), in order to be conservative. The results for standard operation with and without chirp-scaling and wavenumber-shifts are presented in Table 1a. Similar results for ping-pong operation are presented in Table 1b.

Notice that a performance gain from 30% to 50% can be achieved by using these improved processing and operating techniques. It should also be emphasized that these results are for the instantaneous performance of the interferometer. Due to the wide-swath capabilities, all imaged points will be revisited from 2 to 4 times within 10 days, so that additional gains in performance can be expected. As presented in the HOTSWG meeting, using optimal interpolation or simple averaging can significantly reduce the error estimated over a repeat cycle.

Potential Design Changes for Future Missions

The Proteus bus puts limitations on the performance of the WSOA which might be alleviated if another bus were used. The foremost restriction is imposed due to the fact that the Proteus bus yaw steers, so that the WSOA can only be fully operational for part of the mission. The temporal coverage characteristics were already presented at the HOTSWG meeting, and are the main reason for which the WSOA/Jason-2 combination can only be regarded as a demonstration mission. This restriction can be alleviated by using a platform which has solar panels with two degrees of freedom, or if a sun-synchronous orbit is deemed acceptable.

The greatest additional restrictions for the WSOA on Jason-2 are placed by the attitude control system. Bus characteristics place restrictions on the moments and products of inertia which can be accommodated, and also on the lowest allowable frequency. The net result of these restrictions is that the interferometric baseline length must be shorter than the limits set by the current state of the art in rigid deployable masts. Preliminary studies at A.E.C. Able have shown that 10 m masts are well within the limits of feasibility and would be able to meet the stability requirements set by WSOA.

Using the parameters for the previous section, but allowing the baseline to be 10 m long, the expected performance is presented in Table 2a and Table 2b.

An additional limitation, at least at the current time, is the amount of power available from the bus. If the duty cycle were allowed to be doubled by doubling the PRF, while maintaining the same peak power and a 6.4m baseline, the performance shown in Table 3a and Table 3b.

Finally, if one both doubles the duty cycle and increases the baseline length to 10 m, one obtains the performance shown in Tables 4a and 4b.

In summary, given a platform with greater capability for tolerating higher moments and products of inertia, or having higher average power capabilities, the performance of the WSOA can rival that of a conventional altimeter without requiring any improvements in currently available technology. Studies at

JPL have shown that there currently exist platforms which could provide a suitable environment to the WSOA. Some of the platforms have been examined for the Ocean Observer Mission studied by IPO.

Is Off-Nadir Altimetry Inherently Limited?

In a private communication, E. Walsh has raised the concern that the angular variations in the backscatter cross section, σ_0, induce unacceptably large errors on the WSOA estimated heights. In this section we address these errors (leaving mathematical details for an appendix) and show that they are a minor contributor to the WSOA error budget.

The main source for Walsh's concern is due to a misunderstanding of the algorithms which are used to estimate the surface height for coherent interferometers, such as WSOA. In an previous design for a non-coherent interferometer [Bush, et al., 1984] [Parsons and Walsh, 1989], the height had been estimated by tracking the centroid of the waveform formed by the power interference pattern. In this case, the height estimation algorithms are analogous to the height estimation algorithms for conventional altimetry: a single height estimate is obtained by tracking a "waveform" consisting of many range samples. The typical size of the waveform in range is 245 m, for the example chosen by Walsh. This corresponds to a ground resolution of about 3 km. As Walsh correctly points out, the angular variations subtended by such an area will cause a significant shift of the waveform centroid. Using this technique, one would obtain height errors which are meter level, which are unacceptable for WSOA science applications.

Coherent interferometers [Rodríguez and Martin, 1992], on the other hand, do not use waveform tracking to obtain a height estimate. Rather, since the complex samples are returned, it is possible to assign an interferometric phase to each range sample, rather to many range samples. This interferometric phase, together with the radar range (which is not estimated, but rather set by the clock accuracy of the system, and the corresponding time tagging of each range sample), can be converted to an estimate of the surface height, following the algorithm described in [Rodríguez and Martin, 1992].

The angular variation of the backscatter cross section will also result in height biases for a coherent interferometer. However, the range of incidence angles will correspond in this case to the angles subtended by the imaged pixel, rather than by the angles subtended by the interferometric lobe. The ratio of these angles is equal to the ratio of the radar intrinsic range resolution to the range subtended by the interferometric lobe, $7.5/245 \approx 0.03$ so that intuitively one expects the effects to be two orders of magnitude smaller than the biases for the incoherent interferometer case.

Appendix C derives the exact value for the biases, and confirming the intuitive argument outlined above. Using formulas derived in that appendix and the WSOA values for the range resolution and the platform height h, following Table 5 shows the expected height biases as a function of wind speed. As can be seen from this table, the expected errors due to the angular variation of the cross section are very small compared to the other contributors to the WSOA error budget, and can therefore be neglected.

Appendix A: Resampling Using the Chirp-Z Transform

If uniform and identical sampling is used for both radar channels, the imaged pixels on the ground will fail to line up exactly due to the slightly different viewing geometry for each channel.
The range difference between the channels is two given by

$$\Delta r \approx B \sin\theta_0 + B \frac{\cos\theta_0}{\tan\theta_0} \frac{\delta r}{r_0} \qquad (1)$$

where B is the interferometric baseline, θ_0 is the angle to a reference point, r_0 is the range to that point, and δr is the range relative to the reference range, and the expansion has been taken to the center of the swath.

Assuming that the first channel is sampled as $r_1 = r_0 + \delta r$, the second channel must be sampled at the ranges

$$r_2 = r_0 + B\sin\theta_0 + (1+\zeta)\delta r$$

where $\zeta = B\cos\theta_0 / (r_0 \tan\theta_0)$. Assuming that constant timing differences are taken care of by suitably choosing the range compression function, the co-registration problem is reduced to sampling the second channel at $(1+\zeta)\delta r$ if the first channel is sampled at δr. This can be accomplished by using the chirp-scaling algorithm [Rabiner, et al., 1969] [Raney, et al., 1994]. The details are given in the following paragraphs.

Assume the transmit signal is given by

$$S(t) = A(t)e^{i\alpha t^2}e^{i\omega_0 t} \qquad 2)$$

In terms of the system bandwidth Δf and the chirp duration T, $\alpha = \Delta f/(2T)$. The received signal from a point target after down-conversion is given by (after removing the shift to the center pixel)

$$S(t) = A(t-\tau_0)e^{i\alpha(t-\tau_0)^2}e^{-2ik_0 r_2}$$

$$\tau_0 = \frac{2}{c}(r_2 - r_0 - B\sin\theta_0)$$

where k_0 is the center frequency wavenumber, r_2 is the second channel range to the point target.

We proceed to apply the chirp scaling algorithm by multiplying the signal prior to range compression by the quadratic phase factor $\exp[i\beta t^2]$ ($\beta = \alpha\zeta$). Range compression and resampling are achieved by convolving the signal with the reference function $\exp[-i(\alpha+\beta)t^2]$, so that the range compressed signal can be written as

$$S(t) = e^{-2ik_0 r_2}\int d\tau \;\; A(\tau-\tau_0)e^{i\alpha(\tau-\tau_0)^2}e^{i\beta\tau^2}e^{-i(\alpha+\beta)(\tau-t)^2} \qquad (3)$$

Defining the point target response as

$$x(t) = \int d\eta \;\; A(\eta)\exp[2i\alpha\eta t] \qquad (4)$$

the return signal can be written after some rearrangement of terms as

$$S(t) = e^{-2ik_0 r_2} e^{-i\alpha(1+\zeta)t^2} e^{i\alpha\tau_0^2} \exp\left[2i\alpha\tau_0\left((1+\zeta)t - \tau_0\right)\right]\chi\left((1+\zeta)t - \tau_0\right) \qquad (5)$$

If $\beta = 0$ (i.e., no chirp scaling), the result at would be

$$S(t') = e^{-2ik_0 r_2} e^{-i\alpha t'^2} e^{i\alpha\tau_0^2} \exp\left[2i\alpha\tau_0(t' - \tau_0)\right]\chi(t' - \tau_0) \qquad (6)$$

If we set $t' = (1+\zeta)t$ (i.e., the correctly resampled signal), we see that the only difference between equations (5) and (6), is a phase factor $e^{-i\beta t^2(1+\zeta)}$ which can be removed after range compression by post-multiplying the signal.

Notice that, in terms of computation, the chirp scaling algorithm does not increase the number of operations during range compression: it merely changes the reference function, which involves no additional computation. The additional computation occurs in the pre- and post-multiplication of the signal by the appropriate chirp functions. This involves merely N complex multiplications, where N is the number of signal samples, while the range compression involves two 5NlogN Fourier transforms and N complex multiplications, so that the resampling is computationally cheap compared to the range compression.

Appendix B: The Wave-Number Shift for WSOA

Given maximum likelihood estimation, the interferometric phase standard deviation, σ_0, is given by

$$\sigma_\Phi = \frac{1}{\sqrt{2N_L}} \frac{\sqrt{1-\gamma^2}}{\gamma} \qquad (7)$$

where γ is the correlation coefficient between the two interferometric channels:

$$\gamma = \frac{\left|\left\langle v^{(1)} v^{(2)*} \right\rangle\right|}{\sqrt{\left\langle v^{(1)} v^{(1)*} \right\rangle \left\langle v^{(2)} v^{(2)*} \right\rangle}} \qquad (8)$$

and $\langle\ \rangle$ denotes ensemble averaging over speckle realizations. The random height error is due to errors in the estimation of interferometric phase, and is given by [Rodriguez and Martin, 1992]

$$\delta h = \frac{r_0 \tan\theta_0}{kB} \sigma_\Phi$$

where r_0 is the range from the platform to the surface, θ_0 is the look angle, k is the electromagnetic wavenumber, and B is the length of the interferometric baseline.

Equation (7) shows that the phase standard deviation can be predicted if the correlation coefficient can be modeled. The return signals after range compression co-registration can be modeled as

$$v^{(1)}(t) = A\int dS \;\; \chi\left(t - 2r_1/c - \Delta\right) G(\phi)s(r,\phi)e^{-2ikr_1} + n_1 \tag{9}$$

$$v^{(2)}(t) = A\int dS \;\; \chi_r\left(t - 2r_2/c - \Delta\right) G(\phi)s(r',\phi)e^{-2ikr_2} + n_2 \tag{10}$$

where A is a constant which depends weakly on range; Δ is a delay introduced to coregister the two channels; χ_r is the system range point target response; ϕ is the azimuth angle coordinate (any point in the surface plane can be defined by its ground range ρ and its azimuth angle ϕ); $G(\phi)$ is the system antenna pattern, which is assumed to be much broader in the range direction than the system range resolution, so that only its azimuth variation must be included; r_1 and r_2 represent the range from the reference and secondary antennas to a point on the surface; n_1 and n_2 represent the thermal noise in channels 1 and 2, respectively, and are assumed to be uncorrelated white noise processes with variance N; and, finally, $s(r',\phi)$ represents the rough surface brightness which is assumed to satisfy

$$\langle s(\mathrm{r})s^*(\mathrm{r}')\rangle = \delta(\mathrm{r} - \mathrm{r}')\sigma_0 \tag{11}$$

where σ_0 is the normalized radar cross section. Equation (11) is consistent with the deep phase approximation in rough surface scattering [Tsang, et al., 1985], which applies when the surface rms roughness is large compared to the wavelength. That approximation is valid for all the systems studied. Notice that we assume that the radar cross section is constant over the radar resolution cell (see Appendix C for a relaxation of this assumption).

To study the effects of the spectral shift algorithm, we introduce the Fourier transform of the range ptr

$$\chi(t) = \frac{1}{2\pi}\int d\omega \;\; e^{i\omega t}W(\omega) \tag{12}$$

and rewrite the equations for the return signal (neglecting for the moment the thermal noise contributions) to obtain

$$v^{(i)}(t) = A\frac{1}{2\pi}\int d\omega \;\; e^{i\omega(t-\Delta)}W(\omega)$$
$$\int dS \;\; e^{-2i\omega r_1/c}G(\phi)s(r,\phi)e^{-2ikr_1} \qquad (13)$$

$$v^{(2)}(t) = A\frac{1}{2\pi}\int d\omega \;\; e^{i\omega(t+\Delta)}W(\omega)$$
$$\int dS \;\; e^{-2i\omega r_2/c}G(\phi)s(r,\phi)e^{-2ikr_2} \qquad (14)$$

The first step of the wavenumber shift algorithm starts by multiplying both of the interferometric signals in the time domain by a phase factor equivalent to the interferometric phase relative to a reference track. Over a localized region, this is equivalent to multiplying by a constant phase factor, and one which varies linearly in time. For our purposes, we will neglect the constant phase term and assume that the first signal is multiplied by a phase factor $\exp[iwt]$, while the second is multiplied by the complex conjugate. The result of multiplying by a phase ramp in the time domain will be to shift the spectrum in the frequency domain. We will choose w to maximize the spectral overlap of wavenumber components over the pixel. After shifting the spectra, both signal are low-passed filter with an FIR filter whose frequency response we will denote by $H(\omega)$. The filter characteristics will be chosen below to reduce the noise introduced by the frequency shift.

After both of these operations, the return signals can be written as

$$v^{(1)}(t) = A\frac{1}{2\pi}\int d\omega \;\; e^{i\omega(t-\Delta)}W(\omega - w)H(\omega)$$
$$\int dS\, e^{-2i(\omega-w)r_1/c}G(\phi)s(r,\phi)e^{-2ikr_1} \qquad (15)$$

$$v^{(2)}(t) = A\frac{1}{2\pi}\int d\omega \;\; e^{i\omega(t+\Delta)}W(\omega + w)H(\omega)$$
$$\int dS\, e^{-2i(\omega+w)r_2/c}G(\phi)s(r,\phi)e^{-2ikr_2} \qquad (16)$$

In order to calculate the interferometric correlation, one must evaluate the expectation value of the channel cross-product:

$$\left\langle v^{(1)}(t)v^{(2)*}(t)\right\rangle = |A|^2\left(\frac{1}{2\pi}\right)^2\int d\omega_1\int d\omega_2 \;\; e^{i(\omega_1-\omega_2)t}e^{i(\omega_1+\omega_2)\Delta}$$
$$W(\omega_1 - w)W^*(\omega_2 + w)H(\omega_1)H^*(\omega_2)F(\omega_1,\omega_2) \qquad (17)$$

where the last function is defined as

$$F(\omega_1,\omega_2)=\sigma_0\int dS\;\; e^{-2i(k_1r_1-k_2\,r_2)}e^{2iw(r_1+r_2)/\;c}G^2(\phi) \tag{18}$$

and $k_i\equiv k+\omega_i/\;\;c$. Notice that equation (11) was used to reduce the double spatial integral to a single integral.

To proceed further, we notice that we can approximate

$$\begin{aligned} r_1-r_2 &\approx B\left[-\sin\theta+\sin\theta(1-\cos\phi)\right] \\ &\approx B\left[-\sin\theta+\sin\theta\frac{\phi^2}{2}\right] \end{aligned} \tag{19}$$

where we have made use of the fact that the azimuth beamwidth of a typical system is much smaller than 1. Expanding about r_0 and $\theta_0=\arccos(H/\;\;r_0)$, this can be further approximated as

$$r_1-r_2\approx B\left[-\sin\theta_0+\sin\theta_0\,\frac{\phi^2}{2}-\cos\theta_0\cos\theta_0\frac{\delta\rho}{r_0}\right] \tag{20}$$

where $\delta\rho=\delta r/\sin\theta_0$ is the deviation in ground range of the surface point from r_0, and terms of order $\left(R/\;\;(\sin\theta_0 r_0)\right)^2$, where R is the system range resolution, have been neglected.

After making the previous approximation and assuming that we are dealing with a narrow-band system so that , one can evaluate the integral to obtain

$$\begin{aligned} F(\overline{\omega},\Delta\omega)=\frac{\rho_0\sigma_0}{2\sin\theta_0}\,e^{2ikB\sin\theta_0}e^{2i\overline{\omega}/cB\sin\theta_0}e^{-2i\Delta\omega r_0/\,c}e^{4i\omega r_0/c} \\ \frac{c}{2}\,2\pi\delta\left(\Delta\omega-2w-\frac{ckB\cos\theta_0}{r_0\tan\theta_0}\right) \\ \int d\phi\;\; e^{-ikB\sin\theta_0\phi^2}G^2(\phi) \end{aligned} \tag{21}$$

where $\Delta\omega=\omega_1-\omega_2$ and $\overline{\omega}=1/2(\omega_1+\omega_2)$.

Notice that if one chooses the spectral shift

$$\omega=-\frac{c}{2}\,\frac{kB\cos\theta_0}{r_0\tan\theta_0} \tag{22)}$$

the phase is constant over the range resolution cell, for a given azimuth, and it is not hard to convince ones self that the is just the shift in frequency required by geometry so that the projected wavenumber on the ground is the same for both channels. After making this choice for the spectral shift one has that the cross-channel product expectation function can be written as

$$\left\langle v^{(1)}(t)v^{(2)*}(t)\right\rangle = |A|^2 \left(\frac{1}{2\pi}\right)\frac{\rho_0\sigma_0}{\sin\theta_0}\frac{c}{2}e^{2ikB\sin\theta_0}e^{4iwr_0/c}$$
$$\int d\omega\ \ e^{2i\omega(-B\sin\theta_0/c-\Delta)}W(\omega-w)W^*(\omega+w)\left|H(\omega)\right|^2$$
$$\int d\phi\ \ e^{-ikB\sin\theta_0\phi^2}G^2(\phi) \qquad 23)$$

Notice that if the coregistration delay Δ is chosen appropriately, the phase term disappears in the first integral. Furthermore, if one chooses $H(\omega)$ to be centered at zero frequency and with a spectral width of $\Delta f - w/\pi$, where Δf is the bandwidth of W, then only the parts of the signal which correlate on the ground contribute to the return, and no additional noise is brought in due to the spectral shift.
Using the previous results, we obtain the following expression for the complex correlation coefficient

$$\frac{\left|\left\langle v^{(1)}v^{(2)*}\right\rangle\right|}{\sqrt{\left\langle v^{(1)}v^{(1)*}\right\rangle\left\langle v^{(2)}v^{(2)*}\right\rangle}} = \gamma_\phi\gamma_N = \gamma \qquad (24)$$

and the angular (γ_ϕ), and noise (γ_N) correlation factors are given by

$$\gamma_N = \frac{1}{1+SNR^{-1}} \qquad (25)$$

$$\gamma_\phi = \frac{\int_{-\pi}^{+\pi} d\phi\ \ \exp\left[-ikB\sin\theta_0\frac{\phi^2}{2}\right]G^2(\phi)}{\int d\phi\ \ G^2(\phi)} \qquad (26)$$

where SNR is the system signal-to-noise ratio.

The result obtained for the correlation function share the angular and noise correlation functions with the results previously presented at the HOTSWG, but the introduction of co-registration and spectral domain shifts have done away with the misregistration and geometric decorrelation terms. The noise decorrelation term, γ_N, is common to the cross-correlation of any two signals with additive uncorrelated white noise. The fact that the angular correlation term cannot be made to disappear like the geometric correlation term is due to the fact that iso-phase difference contours are hyperbolas, whereas iso-range contours are circles, so that the projected wavelengths can only be made to coincide along one given azimuth direction.

Appendix C: Mathematical Details of σ_0 Angular Variations

The interferometric signal can be modeled as

$$\langle v_1 v_2^* \rangle = A \int dx \; e^{-i\Phi(x)} \sigma_0(x) \chi(x - x_0) \tag{27}$$

where v_i is the coherent signal in channel i, A is a constant which is not important for the following discussion, x is the cross-track distance from the interferometer ground track, $\Phi(x)$ is the interferometric phase difference, which is given by

$$\Phi = kB\sin\theta = kB\frac{x}{r} = kB\frac{x}{\sqrt{h^2 + x^2}} \tag{28}$$

where $k = 2\pi/\lambda$ is the EM wavenumber ($\lambda \approx 2.5$ cm for WSOA), B is the baseline length (7 m for WSOA), θ is the look angle, r is the range, and h is the height above the ocean (1336 km for WSOA).

Following Walsh (and geometric optics), I will take the angular variation of σ_0 to be given by

$$\sigma_0 = ae^{-\theta^2/s^2} \tag{29}$$

where a is a constant independent of look angle, and s^2 is the mean squared slope, which, following Walsh, we will assume to be related to the 10 m wind speed, U_{10}, as follows

$$s^2 = 0.018U_{10}^{1/2} \tag{30}$$

where U_{10} is measured in meters/second.

Finally, $\chi(x)$ is the system range point target response (ptr) as a function of the cross-track distance, and x_0 is the pixel center location. In order to simplify the algebra in the following discussion, I will assume that the ptr can be represented as a Gaussian, as follows

$$\chi(x) = \exp\left(-4(\ln 2)\frac{x^2}{X^2}\right) \tag{31}$$

where X represents the half-power ground resolution (i.e.; $\chi(X/2) = 1/2$), and is related to the system range resolution R by the equation $X = R/\sin\theta$. For WSOA, the system range resolution R is 7.5 m, which corresponds to a bandwidth of 20 MHz.

In order to proceed, we note that for the system parameters used for WSOA, the phase and cross section variations over a pixel are small, so that one is justified in expanding the integral in equation (27) about x_0. Keeping up to first order terms in the Taylor expansion, one readily shows that

$$\Phi \approx kB\sin\theta_0 + \kappa\eta \tag{32}$$

where $\sin\theta_0 = x_0 / \sqrt{h^2 + x_0^2} = x_0 / r_0$, $\eta = x - x_0$, and the cross-track interferometric fringe wavenumber κ is given by

$$\kappa = \frac{kB}{r_0}\cos^2\theta_0 \tag{33}$$

Similarly, one can show that σ_0 can be expanded as

$$\sigma_0(\theta) \approx \sigma_0(\theta_0)\left[1 + \beta\eta\right] \tag{34}$$

where β is given by

$$\beta = -\frac{2\theta_0}{s^2}\frac{\cos\theta_0}{r_0} \tag{35}$$

Introducing these approximations, equation (27) can be written as

$$\left\langle v_1 v_2^* \right\rangle = Ae^{-i\Phi(\theta_0)}\sigma_0(\theta_0)\int d\eta\ e^{-i\kappa\eta}(1+\beta\eta)\chi(\eta) \tag{36}$$

The integral can be evaluated by using the following trick

$$\int d\eta\ e^{-i\kappa\eta}(1+\beta\eta)\chi(\eta) = \left(1 + i\beta\frac{\partial}{\partial\kappa}\right)\int d\eta\ e^{-i\kappa\eta}\chi(\eta) \tag{37}$$

and noticing that the integral in the right hand side of equation (37) is just the Fourier transform of the ptr, which I will denote by $\tilde{\chi}(\kappa)$. The interferometric return can then be written as

$$\left\langle v_1 v_2^* \right\rangle = Ae^{-i\Phi(\theta_0)}\sigma_0(\theta_0)\tilde{\chi}(\kappa)\left(1 + i\beta\frac{\tilde{\chi}'(\kappa)}{\tilde{\chi}(\kappa)}\right) \tag{38}$$

where $\tilde{\chi}'(\kappa) = \partial\tilde{\chi}(\kappa)/\partial\kappa$. With the exception of the expression contained in the last parenthesis of equation (38), this equation represents the expected interferometric return when there is no angular variation of the backscatter cross section. Therefore, all phase (and consequently, height) errors will be introduced by the expression contained in the last parenthesis. In general, the term proportional to β will be much smaller than 1 (as can be verified by inserting an expression for the ptr), and one may approximate

$$\left(1 + i\beta\frac{\tilde{\chi}'(\kappa)}{\tilde{\chi}(\kappa)}\right) \approx \exp\left[\, i\beta\frac{\tilde{\chi}'(\kappa)}{\tilde{\chi}(\kappa)}\,\right] \equiv \exp\left[-i\,\delta\Phi\right] \tag{39}$$

where $\delta\Phi$ is the phase error induced by changes in the cross section as a function of incidence angle. Using equations (31), (33), (35), and the fact that the Fourier transform of a Gaussian is itself a Gaussian, one can show that the phase error as a function of incidence angle is given by the following expression

$$\delta\Phi = -\frac{R^2}{r_0^2}\frac{1}{4\ln 2}\frac{kB\cos\theta_0}{\tan^2\theta_0}\frac{\theta_0}{s^2} \qquad (40)$$

In order to translate this phase error into a height error, we recall that the two are related by the following equation

$$\delta h = \frac{r_0\tan\theta_0}{kB}\delta\Phi \qquad (41)$$

Using equation (40), this can be written as

$$\delta h = -\frac{R^2}{r_0}\frac{1}{4\ln 2}\frac{\cos\theta_0}{\tan\theta_0}\frac{\theta_0}{s^2} \qquad (42)$$

For the range of incidence angles used by WSOA ($\theta_0 < 4°$), one can approximate $\tan\theta_0 \approx \theta_0$ and $\cos\theta_0 \approx 1$, so that the final expression for the height error is given by

$$\delta h = -\frac{R^2}{h}\frac{1}{4\ln 2}\frac{1}{0.018U_{10}^{1/2}} \qquad (43)$$

where I have replaced the mean squared slope by its wind speed dependent equivalent, as given in equation (30).

Acknowledgements. We would like to thank Ed Walsh for expressing his concern and quantifying the errors for the incoherent interferometer case. We would also like to thank E. Thouvenot (CNES) and his colleagues in CNES and Alcatel for helping us to characterize the Proteus bus roll spectrum.

References

Bush, G.B., E.B. Dobson, R. Matyskiela, C.C. Kilgus, and E.G. Walsh, 1984: An Analysis of a satellite multibeam altimeter. *Marine Geodesy*, **8**(1-4), 345-384.

Gatelli, F., A. Monti-Guarnieri, F. Parizzi, P. Pasquali, C. Prati, F. and Rocca, 1994: The wavenumber shift in SAR interferometry. *IEEE Trans. Geoscience & Rem. Sens.*, **32**(4) 855-865.

Parsons, C.L., and E.J. Walsh, 1989: Off-nadir radar altimetry. *IEEE Trans. Geoscience and Rem. Sens.*, **27**(2), 215-224.

Rabiner, L., R. Schaffer, and C. Rader, 1969: The chirp-z transform and its applications. *Bell Syst. Tech. J.*, **48**, 1249-1292.

Raney, R.K., H. Runge, R. Bamler, I. Cumming, and F. Wong, 1994: Precision SAR processing using chirp scaling. *IEEE Trans. Geoscience and Rem. Sens.*, **32**, 786-789.

Rodríguez, E., and J.M. Martin, 1992: Theory and design of interferometric synthetic aperture radars. *IEEE Proc.-F Radar and Signal Proc.*, **139**(2), 147-159.
Rodriguez, E., B.D. Pollard, and J.M. Martin, 2001: Wide-Swath Ocean Altimetry using radar interferometry. *IEEE Trans. Geoscience & Rem. Sens.*, in press.
Tsang, L., J.A. Kong, and R.T. Shin, 1985: Theory of Microwave Remote Sensing. Wiley-Interscience, New York.

Cell Center (km)	Height Error (cm)	Height Error Spectral Shift (cm)
22.1	5.2	3.9
36.4	4.7	3.6
50.7	4.5	3.5
65.0	4.6	3.8
79.2	5.2	4.3
93.5	6.5	5.4

Table 1a: 6.4 m Baseline Height Noise Performance for Single-Transmit Operation

Cell Center (km)	Height Error (cm)	Height Error Spectral Shift (cm)
22.1	5.6	4.1
36.4	4.3	3.3
50.7	3.7	2.9
65.0	3.5	2.8
79.2	3.9	3.1
93.5	4.8	3.9

Table 1b: 6.4 m Baseline Height Noise Performance for Ping-Pong Operation

Cell Center (km)	Height Error (cm)	Height Error Spectral Shift (cm)
22.1	4.4	3.1
36.4	3.7	2.7
50.7	3.4	2.5
65.0	3.3	2.6
79.2	3.8	2.9
93.5	4.6	3.6

Table 2a: 10 m Baseline Height Noise Performance for Single-Transmit Operation

Cell Center (km)	Height Error (cm)	Height Error Spectral Shift (cm)
22.1	5.2	3.3
36.4	3.6	2.6
50.7	3.0	2.2
65.0	2.7	2.1
79.2	2.9	2.2
93.5	3.5	2.6

Table 2b: 10 m Baseline Height Noise Performance for Ping-Pong Operation

Cell Center (km)	Height Error (cm)	Height Error Spectral Shift (cm)
22.1	3.7	2.8
36.4	3.3	2.5
50.7	3.2	2.5
65.0	3.2	2.7
79.2	3.7	3.0
93.5	4.6	3.8

Table 3a: 6.4 m Baseline, Double Duty Cycle, Height Noise Performance for Single-Transmit Operation

Cell Center (km)	Height Error (cm)	Height Error Spectral Shift (cm)
22.1	4.0	2.9
36.4	3.0	2.3
50.7	2.6	2.0
63.0	2.4	2.0
79.2	2.7	2.2
93.5	3.4	2.7

Table 3b: 6.4 m Baseline, Double Duty Cycle, Height Noise Performance Ping-Pong Operation

Cell Center (km)	Height Error (cm)	Height Error Spectral Shift (cm)
22.1	3.1	2.2
36.4	2.6	1.9
50.7	2.4	1.7
65.0	2.3	1.8
79.2	2.7	2.0
93.5	3.3	2.5

Table 4a: 10 m Baseline, Double Duty Cycle, Height Noise Performance for Single-Transmit Operation

Cell Center (km)	Height Error (cm)	Height Error Spectral Shift (cm)
22.1	3.6	2.3
36.4	2.6	1.8
50.7	2.1	1.5
65.0	1.9	1.5
79.2	2.1	1.5
93.5	2.5	1.8

Table 4b: 10 m Baseline, Double Duty Cycle, Height Noise Performance for Ping-Pong Operation

U_{10} (m/s)	Height Error (cm)
1	0.08
7	0.03
10	0.03
15	0.02

Table 5: Height error due to brightness variations, as a function of wind speed.

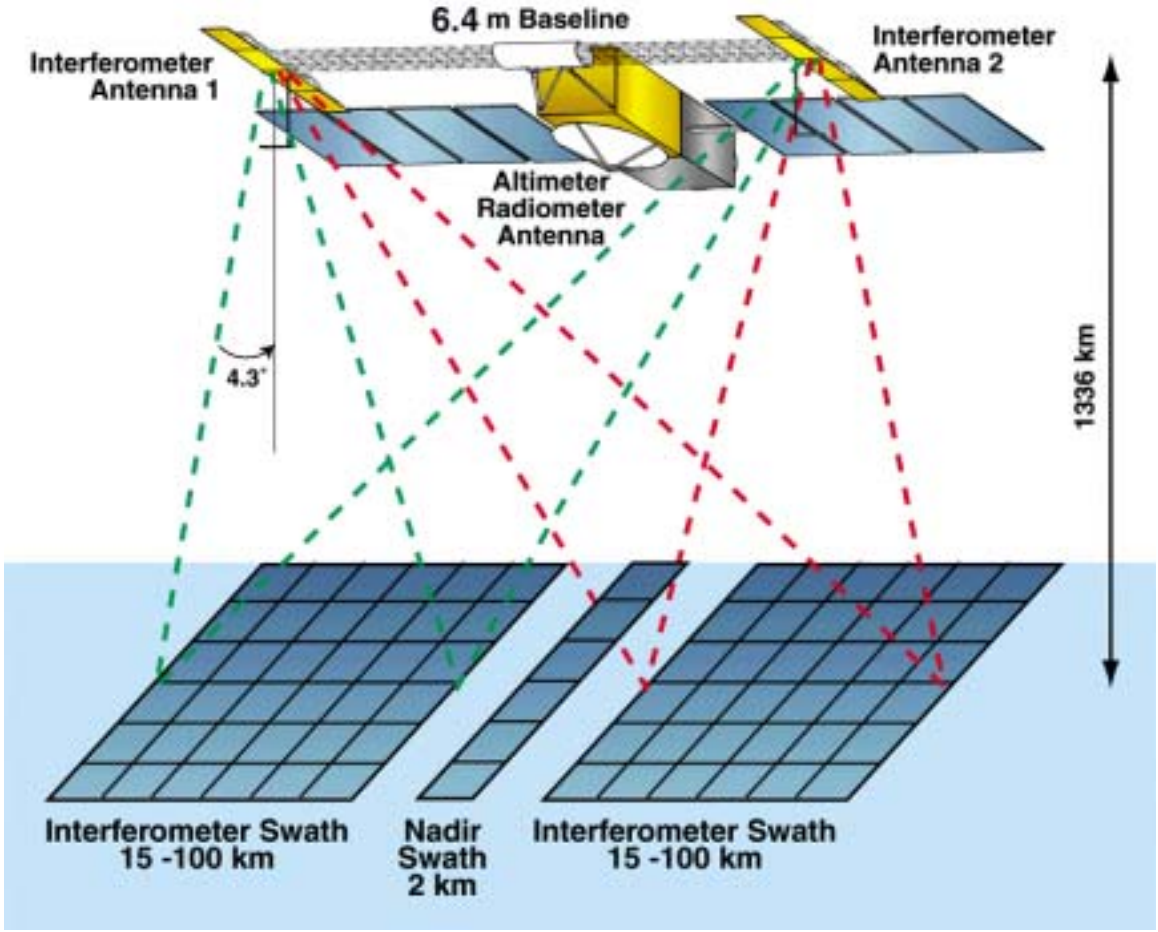

Figure 1. Wide Swath Ocean Altimeter measurement concept. TheWSOA is shown here integrated with the Jason Altimeter and the Proteus bus.

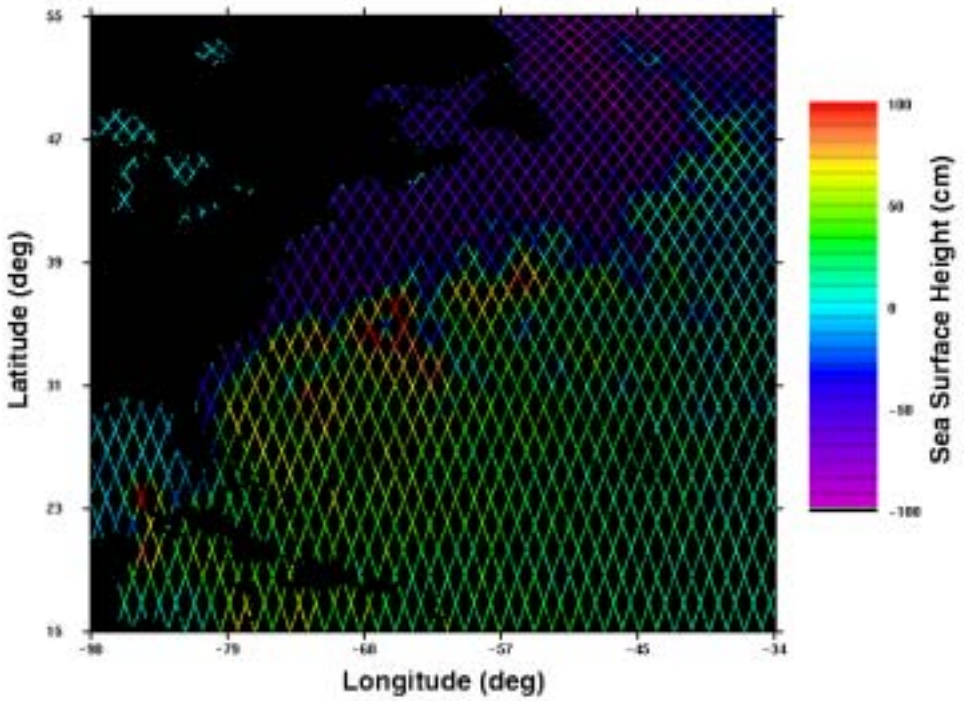

Figure 2a. Example coverage of the North Atlantic for two TOPEX class altimeters flying in formation with an equatorial separation of 150 km.

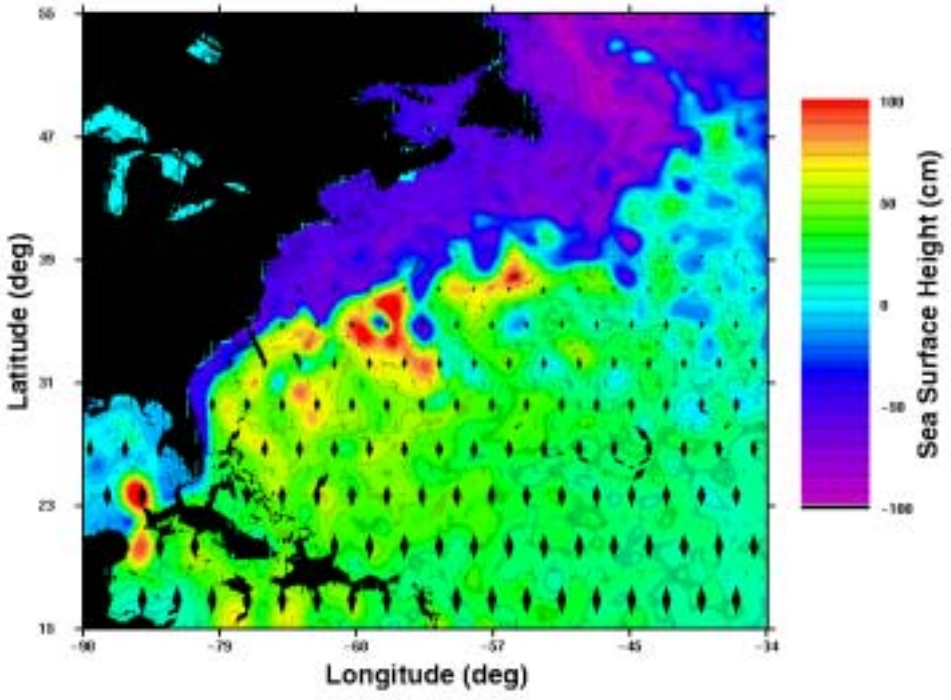

Figure 2b. Simulated estimated heights by a single WSOA in a TOPEX orbit. The height field shown includes measurement noise and residual calibration errors.

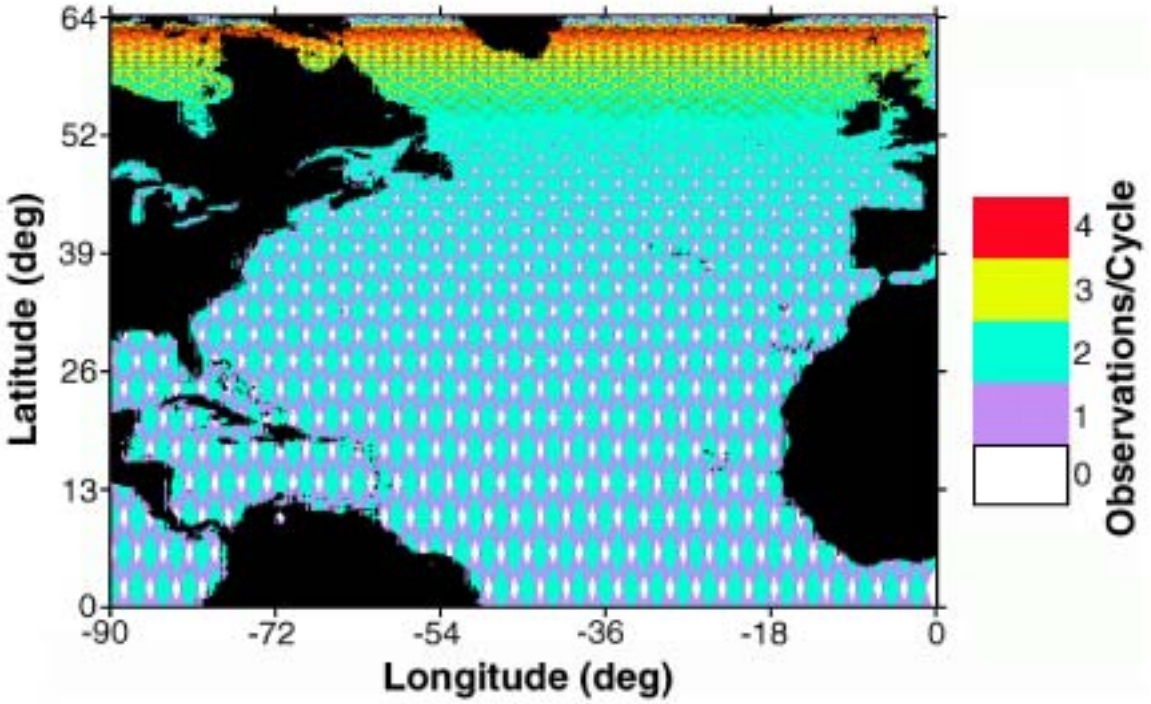

Figure 3. Number of times each surface point is mapped by WSOA during a 10 day repeat cycle. Unlike conventional altimeters, most points in the ocean are mapped at least twice, and often more frequently.

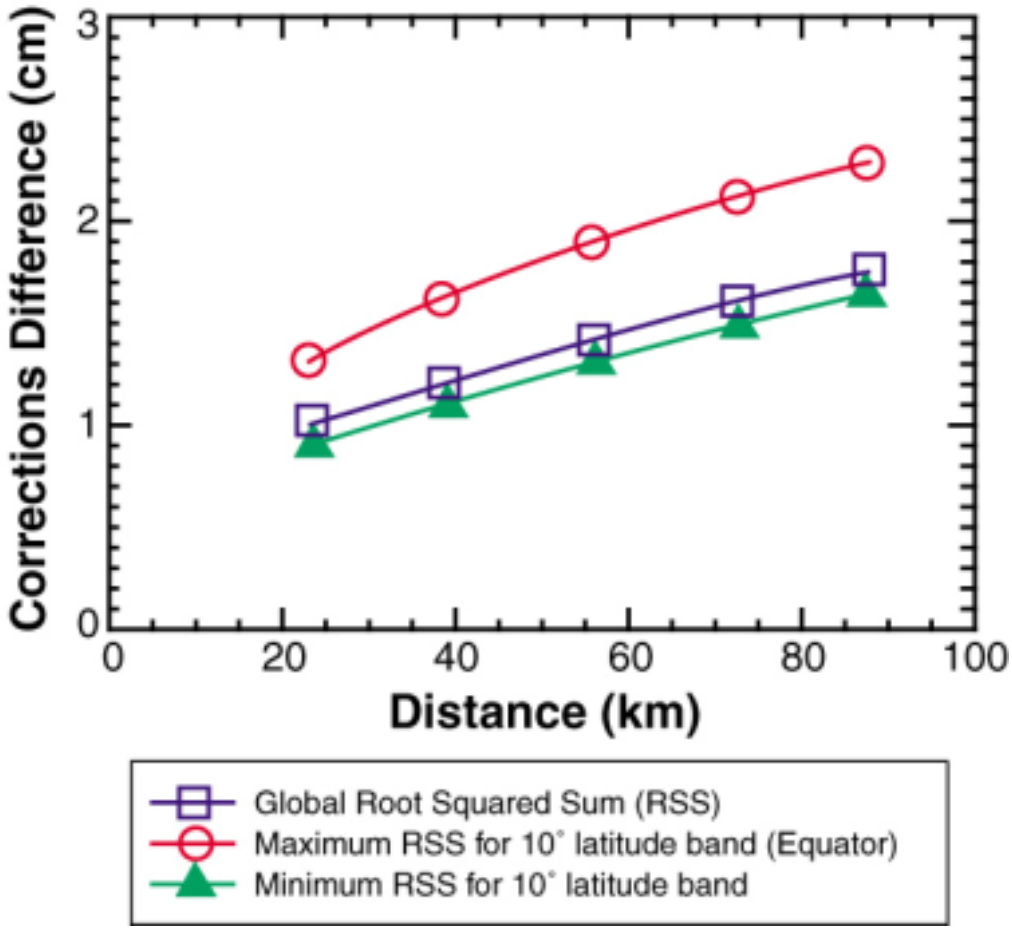

Figure 4. Contribution of tropospheric, ionospheric, and EM bias error sources as a function of distance from the satellite nadir track. The estimates were derived from TOPEX measurements.

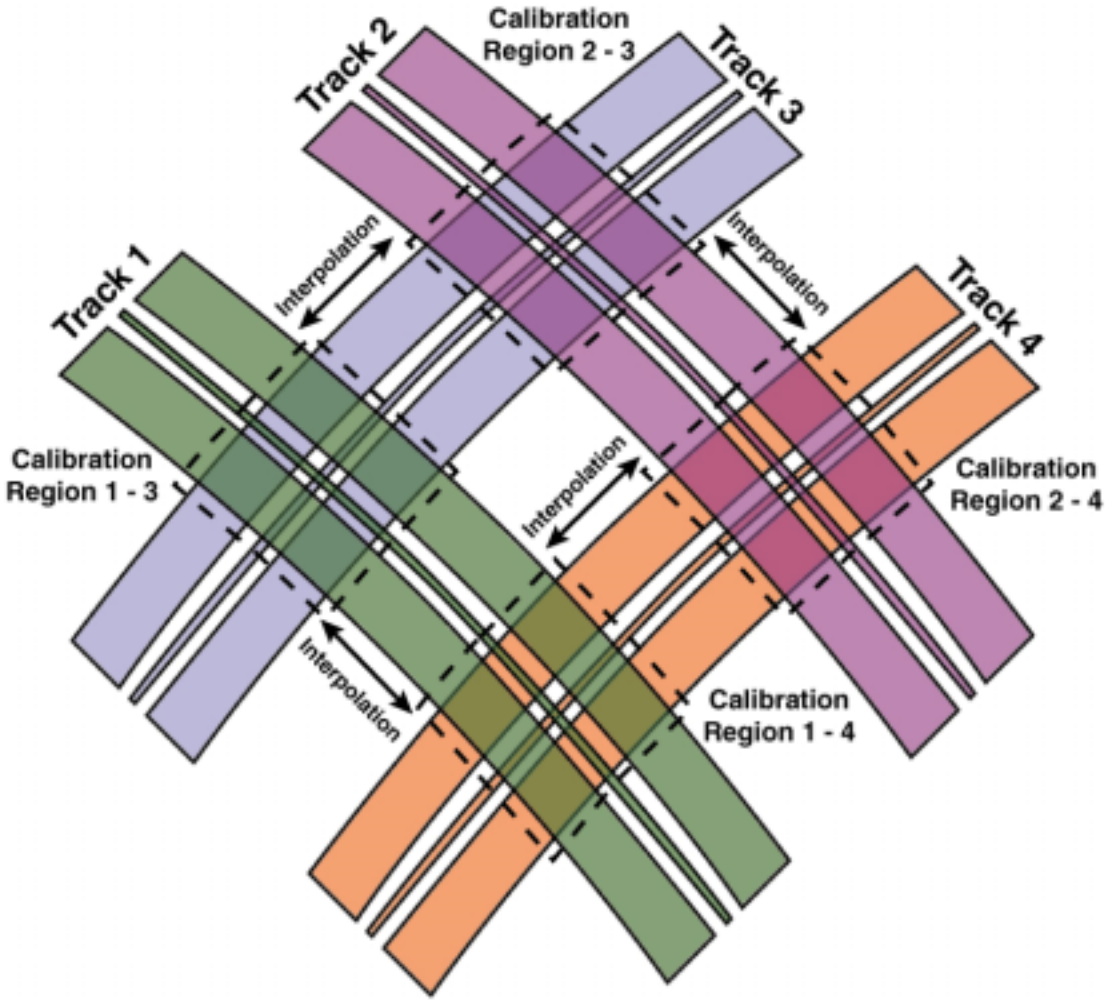

Figure 5. Schematic of the proposed calibration scheme for removing spacecraft roll errors using interferometer and altimeter cross-overs. Assuming four passes, there will be four cross-over regions where the spacecraft roll can be estimated. The estimates of roll are then interpolated between cross-over regions.

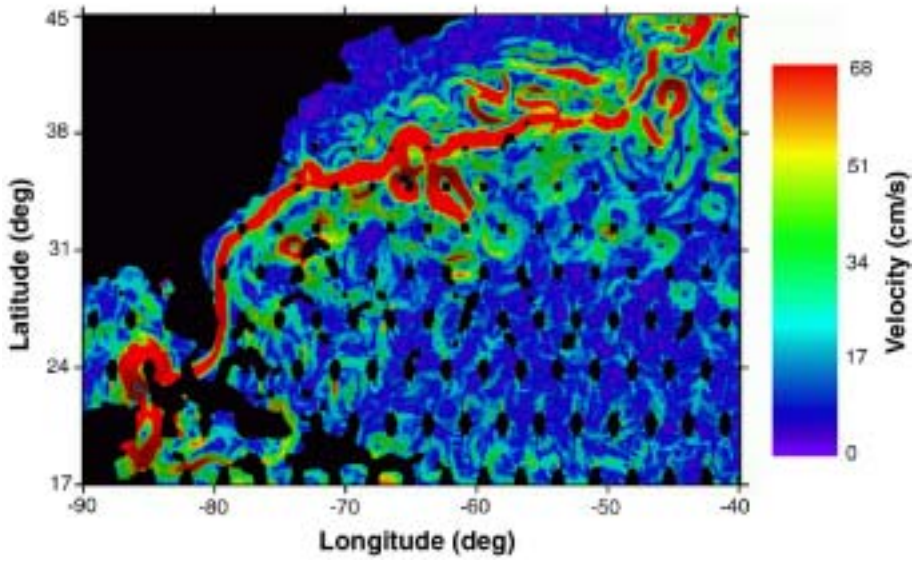

Figure 6a. Magnitude of the geostrophic velocity estimated from the WSOA height simulation results shown in Figure 2a.

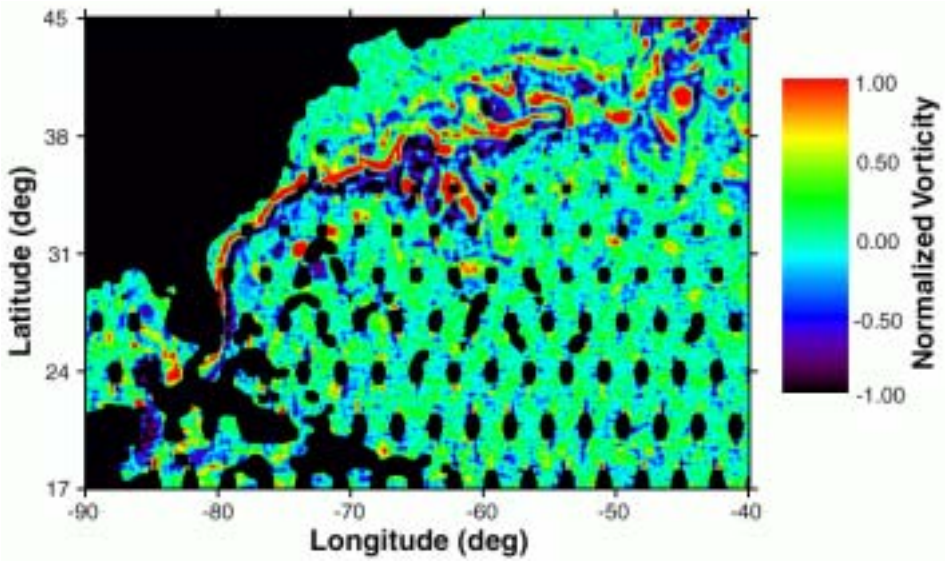

Figure 6b. Relative vorticity estimated from the WSOA height simulation results shown in Figure 2a.

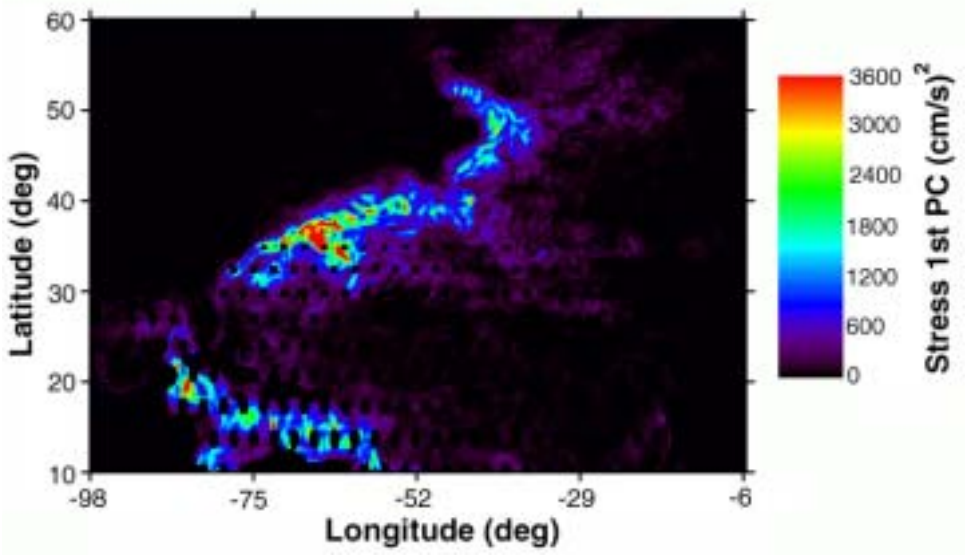

Figure 6c. Principal component of the Reynolds stress tensor, derived from a six month WSOA simulation of the North Atlantic, based on the LANL North Atlantic eddy resolving model.

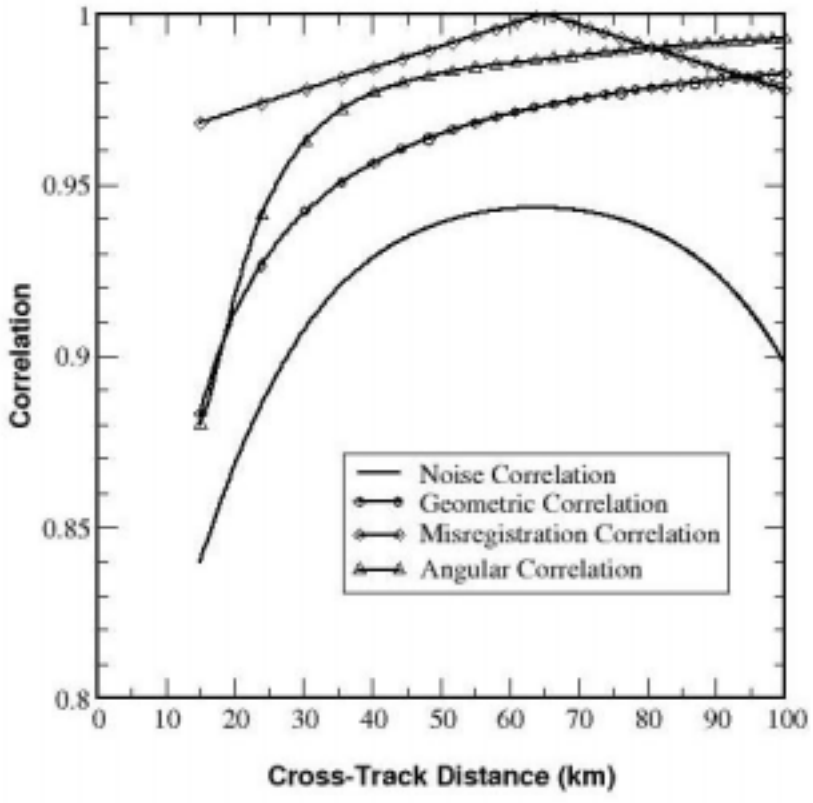

Figure 7. Components of the total correlation between the two interferometric channels assuming the simplest onboard processing. Using the more sophisticated algorithms described in the text, the misregistration and geometric correlations can be neglected. The total correlation is the product of all correlations, and determines the instrument height noise.